Annals of Nuclear Energy 83 (2015) 386–397

Contents lists available at ScienceDirect

Annals of Nuclear Energy

journal homepage: www.elsevier.com/locate/anucene

1/3D modeling of the core coolant circuit of a PHWR nuclear power plant

Santiago Corzo [a,b,*], Damian Ramajo [a,1], Norberto Nigro [a,1]

[a] Research Center for Computational Methods CIMEC-UNL-CONICET, Colectora ruta 168, paraje el pozo, 3000 Santa Fe, Argentina
[b] Nuclear Regulatory Authority ARN, Av. Libertador 8250, C1429BNP Buenos Aires, Argentina

ARTICLE INFO

Article history:
Received 22 September 2014
Received in revised form 19 December 2014
Accepted 20 December 2014
Available online 15 April 2015

Keywords:
1/3D modeling
PHWR
Flow and thermal distribution

ABSTRACT

A multi-dimensional computational fluid dynamics (CFD) one-phase model to simulate the in-core coolant circuit of a pressurized heavy water reactor (PHWR) of a nuclear power plant (NPP) was performed. Three-dimensional (3D) detailed modeling of the upper and lower plenums, the downcomer and the hot and cold leg nozzles was combined with finite volume one-dimensional (1D) code for modeling the behavior of all the 451 coolant channels. Suitable functions for introducing the distributed (friction losses) and concentrated (spacer grids, inlet restrictors and outlet throttles) pressure losses were used to consider the local pressure variation along the coolant channels. The special power distribution at each coolant channel was also taken into account. Results were compared with those previously obtained with a 0/3D model getting more realistic temperature patterns at the upper plenum. Although the present model is restricted to one-phase phenomena, the prediction of the local pressure and temperature along the channels allows for a preliminary identification of the location of incipient boiling by comparing with the local saturation temperature. The present model represents an improvement with respect to the previous 0/3D model. It corresponds to the necessary step before achieving a 1/3D two-phase model with which the pressure drop and subcooled boiling along the coolant channels as well as the overall reactor pressure vessel (RPV) void fraction distribution can be evaluated more accurately.

1. Introduction

The currently being built nuclear power plant (NPP) Atucha II (CNA II), is a pressurized heavy water reactor (PHWR) with a projected total thermal power of 2160 MWt and electric power of 745 MWe. In contrast to the pressure tube type CANDU reactors, CNA II is a pressure vessel type. The core has a vertical configuration housing 451 cooling channels (CC) housed in the moderator tank. Each CC has the aim to remove the thermal power generated by fission of atoms through a coolant flow pumped under high pressure from the lower-plenum to the upper-plenum. The fuel bundles are composed by a set of 37 fuel rods of 5.3 m active length with 13 spacer grids to strengthen and lining up the fuel assembly. The CCs are arranged in a 272 mm trigonal lattice pitch within the moderator tank. CNA II will employ a fuel composed of natural uranium and deuterium (D_2O) heavy water (HW) for cooling and moderation purposes. During normal operation the fuel elements follow a replacement strategy, in which their position is periodically changed with the aim to control burnup.

The NPP Atucha I (CNA I) and CNA II are one of a kind NPP around the world. CNA I is in operation since 1974 and therefore, valuable experience has been gained. However, CNA II is two times larger than the first one, resulting in a technological challenge. For this reason, the main objective of this study is to provide useful information about the thermo-hydraulic behavior in the reactor pressure vessel (RPV) of CNA II.

A 3D drawing of the coolant circuit of CNA II is shown in Fig. 1. In each one of the two loops the hot coolant flows through the hot leg from the RPV to the steam generator to transfer the heat to the secondary circuit. After that, the cold coolant flows to the pump to recover the high pressure and then it returns to the RPV through the cold leg.

The two pair of hot and cold legs are placed diametrically opposed in the RPV. The secondary circuit of light water (LW) is preheated by extracting heat from the moderator circuit and then its temperature continues to rise in the steam generators so as to obtain steam in saturated conditions.

The coolant circuit inside the RPV can be divided into two main reservoirs, the downcomer and lower plenum and the upper

* Corresponding author at: Research Center for Computational Methods CIMEC-UNL-CONICET, Colectora ruta 168, paraje el pozo, 3000 Santa Fe, Argentina. Tel.: +54 342 4511594.
E-mail addresses: santiagofcorzo@gmail.com (S. Corzo), dramajo@santafe-conicet.gov.ar (D. Ramajo).
[1] Tel.: +54 342 4511594.

http://dx.doi.org/10.1016/j.anucene.2014.12.035
0306-4549/

Glossary

NPP	nuclear power plant
CNA	nuclear power plant Atucha
PHWR	pressurized heavy water reactor
PWR	pressurized water reactor
0D	zero-dimensional
1D	one-dimensional
3D	three-dimensional
CC	coolant channel
HZ	hydraulic zone
RPV	reactor pressure vessel
MFR	mass flow rate
NPP	nuclear power plant
CFD	computational fluid dynamics
LOCA	loss of coolant accident
LW	light water
HW	heavy water
SSP	sink/source point
PISO	pressure implicit with split operator
SIMPLE	Semi-Implicit Method for Pressure-Linked Equations
PIMPLE	hybrid PISO/SIMPLE algorithm
VFM	volume finite method
UFR	User Fortran Routine
x	axial position
U	velocity
p	pressure
T	temperature
T_{sat}	saturation temperature
ρ	density
g	gravity acceleration
h	enthalpy
$\bar{\bar{\tau}}$	stress tensor
μ	dynamic viscosity
κ	thermal conductivity
S_S	mass sink/source
S_M	momentum sink/source
S_E	energy sink/source
k	turbulent kinetic energy
ε	turbulence dissipation rate
μ_t	turbulent viscosity
G_t	turbulence production
η	wall roughness
C_f	Darcy friction factor
C_{sp}	pressure drop coefficient at spacer grid
C_{ir}	pressure drop coefficient at inlet restrictor
C_{ot}	pressure drop coefficient at outlet throttle
S_f	pressure drop by wall friction
S_{sp}	pressure drop by the spacer grids of the coolant channel
S_{ot}	pressure drop by the outlet throttle of the coolant channel
S_{ir}	pressure drop by the inlet restrictor of the coolant channel
S_{ps}	power source
D_h	hydraulic diameter
Re	Reynolds number
V_p	cell volume
A_f	cell flow area

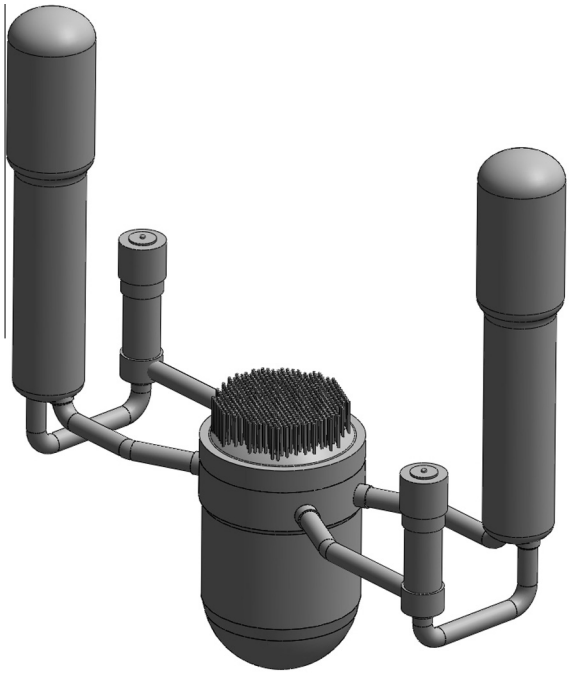

Fig. 1. CNA II main coolant circuit of the PHWR.

plenum, both connected through the CCs and the bypass tubes which transport less than 3% of the total flow. The coolant enters to the RPV through two cold legs and travels down towards to the lower plenum through the annular downcomer between the pressure vessel and the moderator tank walls. Fig. 2 shows a cross section view combining two cutting planes to visualize one hot leg and one cold leg of the RPV (left).

The coolant enters to the CCs through inlet nozzles placed at the lower plenum. The 451 CCs are grouped in 5 hydraulic zones (HZ) with different mass flow rate (MFR) attending to the radial power distribution of the reactor. This in-core flow distribution is mainly produced by flow restrictions placed at some of the CC inlets. Then, the coolant flow is directed upwards through the CCs where the fission heat is extracted and later on it flows towards the upper plenum through vertical slots situated at the CC tubes (outlet throttles). The pressure drop along the CCs is mainly caused by concentrated form losses (sudden area change) at the inlet nozzles, the outlet throttles and the spacer grids. Therefore, friction losses along the fuel rod and tube channel walls are also significant for the HZ with the highest MFR. The expected pressure drop for the coolant flow along the CCs shall be around 6 bar, while the total pressure drop along the whole RPV is around to be around 7.3 bar.

The lower plenum has a flow distributor composed of rhomboidal cells housing the CC inlets. Each cell can group up to 9 CCs (see Fig. 2right). The upper plenum has a convex ellipsoidal shape housing 9 hafnium and 9 steel control rods. Moreover, the upper plenum is crossed by the 451 CC tubes and the moderator inlet and outlet ducts. All these components affect the flow and the thermal distribution in the upper plenum.

In Fig. 2, the scratched solids above the upper and below the lower plenums are the filling bodies, which serve to reduce the coolant inventory in the reactor coolant circuit.

Fig. 3 shows the HZ distribution. The HZ 5 is the most important one, containing 253 of the 451 CCs with around 70% of the total coolant flow. The main aim of the in-core flow distribution is to obtain a balance between the fission heat released and the MFR in each CC.

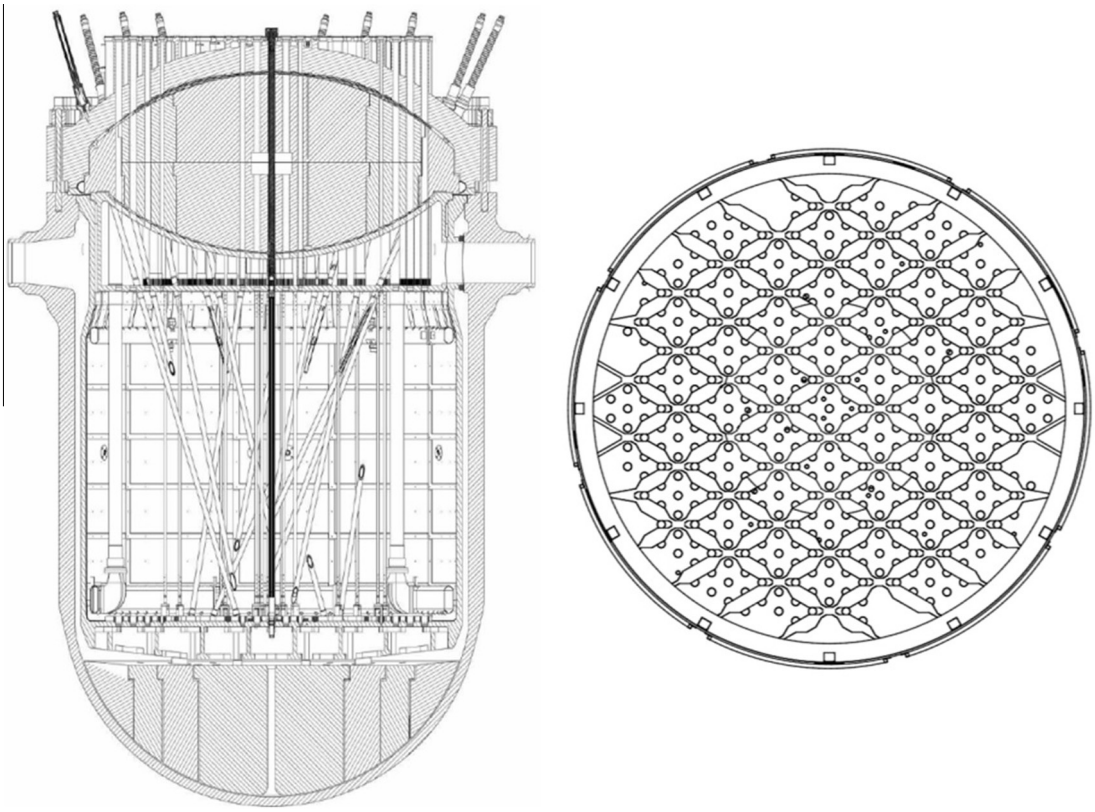

Fig. 2. *Left:* cross sectional cuts of the RPV. *Right:* sketch of the rhomboidal flow distributor at the lower plenum and the location of the CCs inlets.

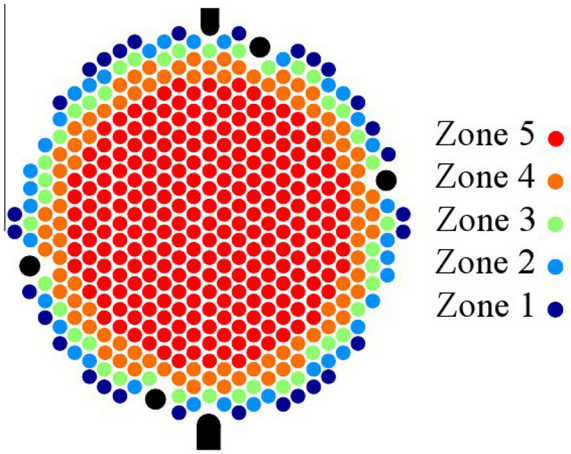

Fig. 3. Hydraulic zones distribution.

Due to the large diameter of the RPV (6.3 m), during the fuel life cycle each fuel bundle is continuously changed from one CC to another CC to control the burnup and the fuel efficiency, until the exhausted fuel is removed from the reactor. The refueling is continuously carried out while the reactor is on-power operation (Adorni et al., 2011). The burnup distribution caused by the refueling and the neutron distribution – because of the large core diameter – produce a radial power pattern along with the typical sinusoidal power pattern along the CCs. Central CCs release around three times more heat power than periphery CCs. Consequently, the in-core flow distribution promoted by the inlet flow restrictions at the CCs must be accurately designed to avoid thermal stratification at the upper plenum and high coolant temperature at the core central zone. In this sense, predictions of the radial

Table 1
Characteristics of the five hydraulic zones.

Property	Hydraulic zone				
	1	2	3	4	5
Total number of CC	30	36	42	90	253
Average channel power (MW)	2.052	2.812	3.837	5.268	6.661
Nominal MFR	9.29	11.70	15.08	21.27	27.73

and axial power distribution were obtained from 0/1D codes and used in this work for CFD simulations. Table 1 summarizes the main characteristics of the five HZ. Note that the channel power limit and the corresponding MFR, are increased almost three times from the HZ 1 to the HZ 5.

Several researchers have focused their efforts to study the pressure drop in specific reactor components, especially in fuel bundles (Le Corre et al., 2010; Vijayan et al., 1999; Anglart et al., 1997). Other authors have developed a discussion about the in-channel thermal and void fraction distribution in pressure water reactors (PWR) (Krepper et al., 2007; Kurul and Podowsky, 1991). On the other hand, there are not many CFD simulations covering the whole coolant flow inside the RPV of a NPP. Zero/One-dimensional (0/1D) transient codes like RELAP5 (Carlson et al., 1990; Chen et al., 1994), ATHLET (Lerchl and Austregesilo, 2006) or COBRA3-CP (Thurgood, 1983) are useful to modeling the overall reactor whilst giving a complete descriptions of the nuclear plants in nominal conditions and operational transients as well as postulated accidents. Although these codes allow a limited understanding of the flow behavior inside the reactor core, they have been useful tools for safety assessment and NPP design for more than three decades. However, these 0/1D approaches are not always satisfactory for simulating 3D transients that can take place in complex components such as in the upper plenum of the RPV (Vyskocil and Macek, 2014). Current CFD simulations of the RPV are limited by

the number of degree of freedoms. Full 3D-CFD models of the RPV considering all the CCs would demand huge meshes with high refinement around the small components such as spacers, fuel bundles and throttles. These models could be very challenging or unable to solve with the current computational resources. A few works concerning to 3D CFD simulations of the coolant flow in an isolated RPV can be found (Tsuji et al., 2014; Jeong and Han, 2008). These works are devoted to determination of the in-core thermal stratification or de heat removal under natural convection during a LOCA event.

Some researchers have carried out simulations of CNA II with different 0/1D nuclear codes. Mascitti and Madariaga (2011) employed the MCNP5 code to calculate the displacement-per-atom (DPA) in order to estimate RPV aging by irradiation embrittlement. Lazarte et al. (2010) validated RELAP5 and TRACE5 codes against experimental facility data in order to assess the fast boron injection system shutdown. Araneo et al. (2010) performed 3D CFD simulations (CFX) in order to investigate the thermal stratification and mechanical stresses under core re-flood during a LOCA event. Mazzantini et al. (2010) used DYNETZ (an specific code developed by KWU for ATUCHA II) for modeling the whole NPP coupled with RELAP5 for modeling each of the 451 CC and PCE code (developed from PUMA code) to solve the local spatial neutron kinetic. The effect of subcooled boiling on the transient power distribution and vise versa was studied.

Adorni et al. (2011) used a dedicated fuel rod thermo-mechanical code (TRANSURANUS) to evaluate the fuel integrity under a 2A LB-LOCA event and it was concluded that the percentage of fuel rods failures is well below 10%.

Bonelli et al. (2012) gave an extended introduction about CNA II installation and MELCOR 1.8.6 was employed to solve a station black-out analysis. Despite of the code limitations (it was developed for PWR and BWR with H_2O properties), the MELCOR model was assessed against a previous RELAP5 model before the postulated black-out event was solved. Recently, Lestani et al. (2014) modeled the fuel bundles of CNA II with the neutron physics cell code WIMSD-5. A different fuel bundle was proposed in order to improve the slightly negative power coefficient of the current fuel bundles.

A recent work (Vyskocil and Macek, 2014) dealt with the coupling of 3D CFD code (Fluent) with ATHLET, which can be internally coupled with Dyn3D (a neutron kinetic code) for solving a light water reactor (VVER-1000 of 1000 MWe). In this case, the primary and secondary circuits were modeled with ATHLET, the flow in the downcomer and lower plenum was simulated by fluent and the heat generation was solved with Dyn3D. The current model is limited to scenarios with a single-phase flow in the CFD domain.

In this work, it is also proposed a multi-dimensional (1/3D) approach coupling 3D domains of the upper plenum, the lower plenum and the downcomer with an in-house 1D code for modeling the pressure drop and heat transfer in each of the 451 CCs. The 1/3D coupling model allows a more detailed description of the coolant circuit of the whole RPV, giving more detail where it is required. The present work corresponds to the second stage for improving an original model in which the CCs were represented by zero-dimensional (0D) heat and momentum balances (Ramajo et al., 2013). Regarding the in-core MFR distribution, the previous 0/3D model has shown similar results than the present 1/3D model. On the other hand, the last has several improvements, mainly by allowing a prediction of the pressure drop and heating along the CCs. The main difference is established in the thermal variables and their effects over the fluid dynamics and thermal properties experiencing large variations because most of the heating process is concentrated in these cooling channels. For this reason, a compressible 1D code model was implemented in the present work.

2. Computational model

The multidimensional methodology was performed by coupling the 1D code for CCs modeling with the 3D domains for the rest of the coolant circuit. The coupling was achieved by the use of ANSYS-CFX and the implementation of a novel strategy of sink/source points (SSPs) developed and assessed for the 0/3D previous model (Ramajo et al., 2013). In this, the lower end of each CC (that is the inlet flow under normal conditions) is represented by a SSP located at the 3D lower plenum domain. Similarly, the upper end of each CC is represented by another SSP located at the 3D upper plenum domain (see Fig. 4).

The information collected from the 3D domains for these two points of each CCs are the boundary conditions for modeling the 1D CC. On the other hand, each CCs returns information about the mass (S_S), momentum (S_M) and energy (S_E) source terms for solving the 3D transport equations. The coupling was implemented using the User Fortran Routine (UFR) tools, which in run time (at the beginning of each iteration of the 3D model) receives the current flow conditions (pressure and temperature) from the upper and lower SSPs of each CC, calculates the requested variables (MFR, temperature and axial velocity) and returns the results to the 3D solver. The 3D to 1D coupling was done in a partitioned way, which is similar to a loose coupling method but with extra inner iterations that forces the solution to converge in a similar way to a strong coupling algorithm, but avoiding the excessive computational cost.

Fig. 4 at the left shows a sketch of the coolant flow and the location of the two SSPs corresponding to one CC. Fig. 4 at the right shows the 451 source points located in the upper plenum.

The 3D domain was made from the assembly of two isolated domains; the upper plenum and the lower plenum, which are joined through the SSPs which transport the conserved variables from one domain to the other. The upper plenum contains a short part of the hot legs, the 22 guide tubes for the control and shut down system rods, the 4 vertical moderator inlets and the 2 elbow moderator outlets. Vertical cylinders were placed above each SSP to represent the extreme of the fuel assembly containing the mechanical coupling system for the refueling operation. As for the lower plenum, a short part of the cold legs, the downcomer and the rhomboidal flow distributor were included.

The neutron's fission heat transferred from the fuel rods to the coolant was included taking into account axial and radial power distributions from previous calculus. The heat transferred from the CC to the moderator tank was estimated as %5 of the total fission power delivered by the fuels.

3. Mathematical formulation

The 3D CFD model is formulated as one-phase Newtonian fluid flow with variable dynamic and thermo-physical properties locally computed as a function of the pressure and temperature using tables for LW and polynomial interpolation functions for HW. For LW, the IAPWS-IF97 database (Wagner and Cooper, 2000) was used. As regards to HW, suitable polynomial functions with pressure and temperature as independent variables were employed for computing the dynamics and thermal properties. The expressions were built from RELAP5 database for a pressure range of 94–130 bar and a temperature range from 195 to 330 °C and implemented in the model using the Command Expression Language tools (CEL) in CFX:

$$\rho(p,T) = 979.3 - 0.5817p + 1.286T + 0.00223p^2 + 0.000763pT - 0.006267T^2 \ [\mathrm{kg\,m^{-3}}] \quad (1)$$

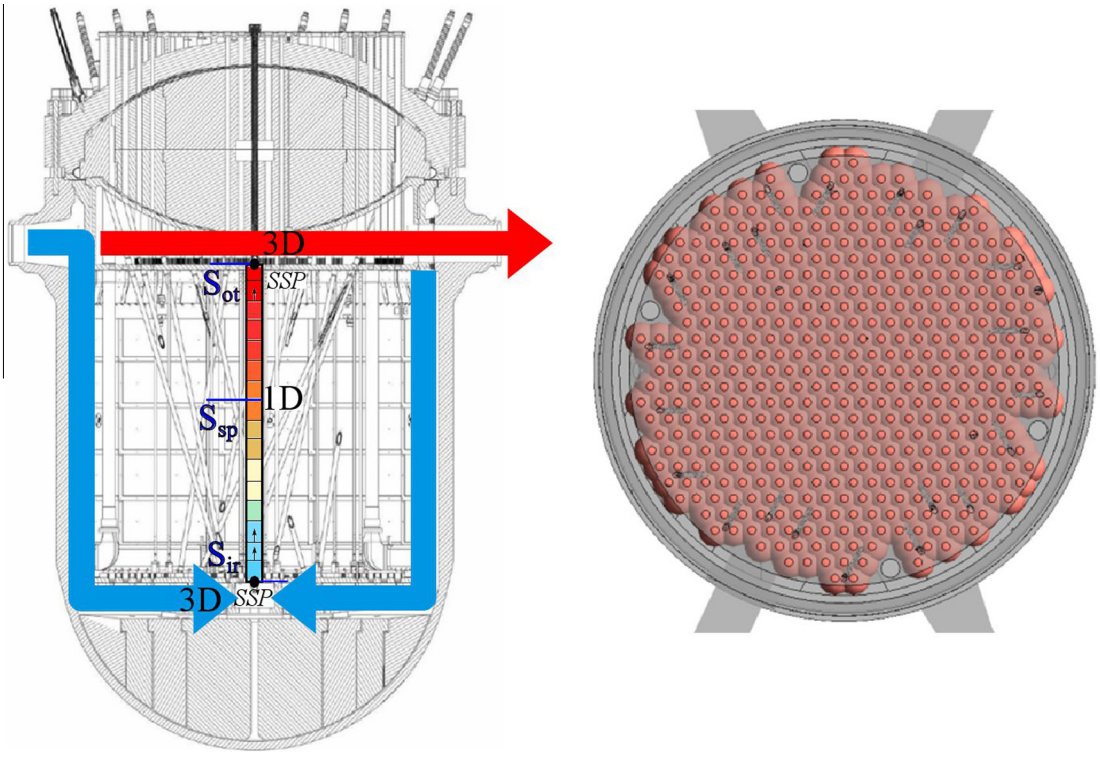

Fig. 4. *Left:* 1/3D couple scheme. *Right:* SSPs in the upper plenum.

$$\mu(p,T) = 0.0003899 + 2.007\times10^{-8}p - 1.601\times10^{-6}T + 1.142\times10^{-10}p^2 - 1.954\times10^{-10}pT + 2.08\times10^{-9}T^2 \text{ [Pa s]} \quad (2)$$

$$C_p(p,T) = 4.583\times10^{-4} - 732.0T + 4.8T^2 - 0.01392T^3 + 1.519\times10^{-5}T^4 \text{ [J kg}^{-1}\text{ C}^{-1}\text{]} \quad (3)$$

Steady state simulations were performed using the finite volume software ANSYS-CFX 13®. For reaching the steady state a time marching integration algorithm was chosen (ANSYS-CFX, 2010). This strategy allows a fictitious time step as a relaxation parameter that smoothly controls the convergence of the strong non linearities. The 1D code was also formulated using Finite Volume Method (FVM) written in Fortran 90 and linked with the CFX solver using the above mentioned UFR tools (ANSYS-CFX, 2010). Pressure based compressible formulation was employed. During the simulations, the fluid compressibility was included through the first of the above expressions which allows the local variation of density as a function of the temperature and pressure to be computed.

3.1. 3D formulation

The governing equations for the 3D model are described in the next paragraphs. The continuity equation takes the following form:

$$\frac{\partial\rho}{\partial t} + \nabla\cdot(\rho U) = S_S \quad (4)$$

where ρ is the density, U is the velocity and S_S is a sink/source term placed at each SSP. Regarding the momentum equation, it can be written as:

$$\frac{\partial(\rho U)}{\partial t} + \nabla\cdot(\rho UU) = -\nabla p + \nabla\cdot\bar{\bar{\tau}} + \rho\bar{g} + S_M \quad (5)$$

where p is the static pressure, $\bar{\bar{\tau}}$ is the shear stress tensor and S_M is the momentum sink/source introduced with the mass flow coming from the CCs models. The pressure–velocity coupling was solved using the Semi-Implicit Method for Pressure-Linked Equations (SIMPLE) (Rhie and Chow, 1983). Density and fluid properties were updated inside the pressure–velocity coupling loop as it is shown below.

The energy balance was accomplished in terms of enthalpy by:

$$\frac{\partial(\rho h)}{\partial t} - \frac{\partial p}{\partial t} + \nabla\cdot(\rho Uh) = \nabla\cdot(\kappa\nabla T) + \nabla\cdot(U\bar{\bar{\tau}}) + S_E \quad (6)$$

where h is the static enthalpy, κ is the thermal conductivity, T is the fluid temperature and S_E is the enthalpy of the mass flow coming from/to the CCs. The standard two equation k–ε model (Launder and Spalding, 1974) was employed to model the turbulence and a standard logarithmic wall law was applied to represent the logarithmic velocity profile near walls, thus avoiding high mesh refinement (ANSYS-CFX Theory guide, 2010). k–ε is extensively employed due to its robustness and suitable accuracy when relatively rough meshes are used. The transport equations for the turbulent kinetic energy k and the turbulence dissipation rate ε are:

$$\frac{\partial(\rho k)}{\partial t} + \nabla\cdot(\rho Uk) = \nabla\left(\frac{\mu_t}{\sigma_k}\nabla k\right) + G_t - \rho\varepsilon \quad (7)$$

$$\frac{\partial(\rho\varepsilon)}{\partial t} + \nabla\cdot(\rho U\varepsilon) = \nabla\left(\frac{\mu_t}{\sigma_\varepsilon}\nabla\varepsilon\right) + \frac{\varepsilon}{k}(C_1G_t - C_2\rho\varepsilon) \quad (8)$$

where μ_t is the turbulent viscosity, which can be obtained from the eddy viscosity model:

$$\mu_t = \frac{C_\mu\rho k^2}{\varepsilon} \quad (9)$$

C_1, C_2, σ_k, σ_ε and C_μ are model constants, being 1.44, 1.92, 1.0, 1.3 and 0.09, respectively.

In Eqs. (7)–(9), G_t is a turbulence production term estimated from the velocity gradient and the turbulent viscosity μ_t as:

$$G_t = \frac{1}{2}\mu_t(\nabla U + (\nabla U)^T) \quad (10)$$

3.2. 1D formulation

The presented model is a considerable improvement with respect to the previous 0D approximation. The main difference are the inclusion of the axial power distribution, the more realistic approximation offered by a 1D channel model against its 0D counterpart, improving the temperature estimation. While the 0D code estimates all coefficients in function of mean values, the present 1D code models the variation of pressure and temperature along the channels and computes the density and thermal and transport properties in each cell of the 1D domains.

For CC modeling, a 1D FVM formulation was implemented. In this case, the Reynolds stress tensor $\left(\nabla\cdot\bar{\bar{\tau}}\right)$ in Eq. (5) is reduced to one component associated with the axial diffusion. However, this effect is small compared with the axial convective flow $(\nabla\cdot(\rho UU))$. Moreover, the wall diffusivity effects and the form pressure losses were modeled using Darcy–Weisbach (Moskva, 1960) equation with empirical correlations, experiments and CFD results. Finally, the mass and momentum transport equations took the following form:

$$\frac{\partial\rho}{\partial t}+\nabla\cdot(\rho U)=0 \tag{11}$$

$$\frac{\partial(\rho U)}{\partial t}+\nabla\cdot(\rho UU)=-\nabla p+S_f+S_{sp}+\rho\bar{g} \tag{12}$$

In Eq. (12), S_f and S_{sp} represent the pressure drops caused by the wall friction and by the spacer grids. The local pressure drop from the inlet flow restrictions and the outlet throttle are included in the boundary conditions. The energy equation is accomplished in terms of the enthalpy variable as:

$$\frac{\partial(\rho h)}{\partial t}-\frac{\partial p}{\partial t}+\nabla\cdot(\rho Uh)=\nabla\cdot(\kappa\nabla T)+S_{ps} \tag{13}$$

In Eq. (13), S_{ps} is the energy source to account for the fission heat release. This single-phase model did not consider the evaporation and condensation. For this reason, the enthalpy could exceed the saturation temperature.

Moderator heating is caused by two effects; neutron moderation and heat transfer by conduction, convection and radiation from the CCs. Despite the low agitation of the moderator flow and the thermo-foils placed at the outer side of each CC to improve insulation, it is expected that the heat transfer rate would be less than 5% of the total fission power. For this reason the total fission power applied in the source term S_{ps} in Eq. (13) was properly reduced.

Density variation due to the temperature and the pressure gradients along the CC are significant. Consequently, it is necessary to take them into account in the transport equations formulation. However, under normal operation slow time variation of density is expected $\left(\frac{\partial\rho}{\partial t}\approx 0\right)$. Thus, a pressure-based formulation was implemented updating the actual density value after each iteration step according to Eq. (1).

The frictional pressure drop in Eq. (12) was computed by Darcy–Weisbach equation:

$$S_f=\left(\frac{dp}{dx}\right)_f=\frac{1}{2}\frac{\rho}{D_h}C_fU^2 \tag{14}$$

where D_h is the hydraulic diameter and C_f is the Darcy friction factor. Many researchers have studied pressure drop in fuel bundles of PHWR (Bae and Park, 2011; Chun and Seo, 2001). The C_f was estimated by the modified Colebrook equation (Ambrosini et al., 2004) for different Reynolds number (Re):

$$C_f=\begin{cases} C_l=\frac{64}{Re} & Re\leqslant 2200\\ C_{lt}=\left(3.75-\frac{8250}{Re}\right)\left(C_{t,3000}-C_{l,2200}\right)+C_{l,2200} & 2200<Re<3000\\ C_t=\left\{2\log\left[\frac{\eta}{3.7D}+\frac{2.51}{Re}\left[1.14-2\log\left(\frac{\eta}{3.7D}+\frac{21.25}{Re^{0.9}}\right)\right]\right]\right\}^{-1/2} & Re\geqslant 3000\end{cases} \tag{15}$$

Similarly, the spacer-grid pressure drop was computed as:

$$S_{sp}=\left(\frac{dp}{dx}\right)_{sp}=\frac{1}{2}\frac{\rho}{dx}C_{sp}U^2 \tag{16}$$

$$S_{res}=\Delta P_{res}=\frac{1}{2}\rho C_{res}U^2 \tag{17}$$

In Eqs. (16) and (17) C_{sp} and C_{res} are the form coefficients for the spacers and inlet restrictors, which depend on the local Re.

Correlations for predicting the pressure drop can be found in literature for several spacer grids (Anglart et al., 1997; Ghiaasiaan, 2008). In this work the C_{sp} coefficients were obtained from CFD simulations previously calculated for the original spacer grid geometry and the flow operation conditions of each hydraulic zone (Corzo et al., 2011). Table 2 summarizes the form and friction coefficients calculated for the nominal mass flow rate and fluid nominal conditions (122 bar and 266 °C) for each HZ. Finally, the outlet throttle pressure loss was estimated by the Darcy–Weisbach equation with a Darcy coefficient (C_{ot}) obtained by CFD (Corzo et al., 2011).

As mentioned above, the restrictions and the outlet throttle losses were explicitly imposed by modifying the boundary condition at the CC ends.

4. Numerical aspects and discretization

The 1D compressible formulation was solved using Finite-Volume Method (FVM) (Versteeg and Malalasekera, 2007) based on the discretization proposed by (Jasak, 1996). The PIMPLE algorithm (hybrid PISO/SIMPLE) (Jasak et al., 2007) was chosen for solving the pressure–velocity coupling. Standard PISO algorithm is not feasible for this kind of flows due to the stringent constraint on the maximum time step imposed by PISO. On the contrary, the PIMPLE algorithm has an improvement in convergence and stability.

The problem was solved using 4 inner and 3 outer PIMPLE iterations. The energy equation was solved in a separate way once the pressure and velocity were updated. The fluid properties (μ, ρ and κ) were updated at the beginning of each outer PIMPLE iteration.

Both Eqs. (14) and (16) have a quadratic non-linear dependence with velocity which could affect the momentum equation stability. There are two possible solutions for this problem; either use a solver for non-linear systems, or linearize these terms (Ferziger and Peric, 1999). For example, the linearized form of Eq. (14) can be written in semi-implicit form as:

$$S_f=\frac{1}{2}\frac{\rho}{D_h}C_fU^2\approx\frac{1}{2}\frac{\rho}{D_h}C_f\left(U^{n-1}U^n\right) \tag{18}$$

Mass and momentum equations are discretized on the staggered control volumes (Eqs. (19) and (20)). Advection terms are written using Gauss theorem:

Table 2
Pressure or loss coefficients for the different CC components.

CC component	Pressure loss coefficients				
Hydraulic zone	1	2	3	4	5
Inlet flow restrictor ($C_{ir,0}$)	879.27	539.45	286.15	79.72	1.09
Outlet throttle (C_{ot})	1.86	1.86	1.86	1.86	1.86
Spacer grids (C_{sp})	14.25	8.55	4.89	1.99	1.14
Fuel rods + channel wall (C_f)	0.0184	0.0175	0.0166	0.0155	0.0147

$$\frac{V_p}{\Delta t}(\rho^n - \rho^{n-1}) + \sum_f (\rho U)_f^n A_f = 0 \tag{19}$$

$$\frac{V_p}{\Delta t}\left(\rho^n U^n - \rho^{n-1}U^{n-1}\right) + \sum_f (\rho U)_f^n U_f^n A_f + \left(\frac{1}{2}\frac{\rho^n}{D_h} C_f U^{n-1} V_p\right) U^n + \left(\frac{1}{2}\frac{\rho^n}{\Delta x} C_{sp} U^{n-1} V_p\right) U^n = \sum_f p_f^n A_f + \rho^n \bar{g}_p^V \tag{20}$$

where V_p and A_f are the cell volume and flow area respectively. Fig. 5 shows schematically the model algorithm and the interaction between both domains. A pair of source points is required for modeling each CC. To accomplish that, each upper source point was placed at the location of the corresponding CC outlet flow throttle. At the same way, each bottom sink point was housed inside the corresponding rhomboidal cell of the flow distributor at the lower plenum. In order to represent better the real geometry, the sink points were located as closer as possible to the top wall of the distributor. Once the coordinates of the points are given to CFX, different user functions (one for each flow variable) are invoked during the simulation in order to extract the flow characteristics at the SSPs. Each SSP implemented is mass-source type. It acts only in the corresponding cell equations. Under normal operation conditions -that is the coolant flowing in upward direction- the upper SSPs represent sources injecting mass into the upper plenum while the bottom SSPs represent sinks extracting mass from the lower plenum. Therefore, the necessary arguments to be communicated to the 1D code are the pressure and the temperature from the bottom SSPs while only the pressure is necessary for the upper SSPs. In case of backflow the boundary conditions are adapted to have a well posed mathematical problem. This flow information is extracted from the 3D domain by means of the *probe(var)@loc* function of

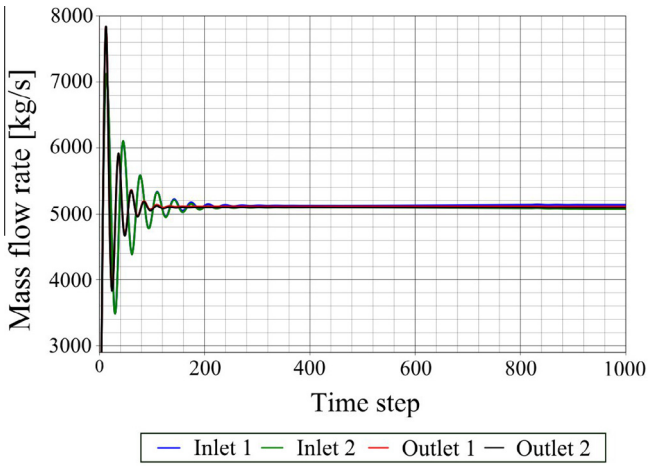

Fig. 6. Mass flow rate at the inlet and outlet boundaries of the RPV.

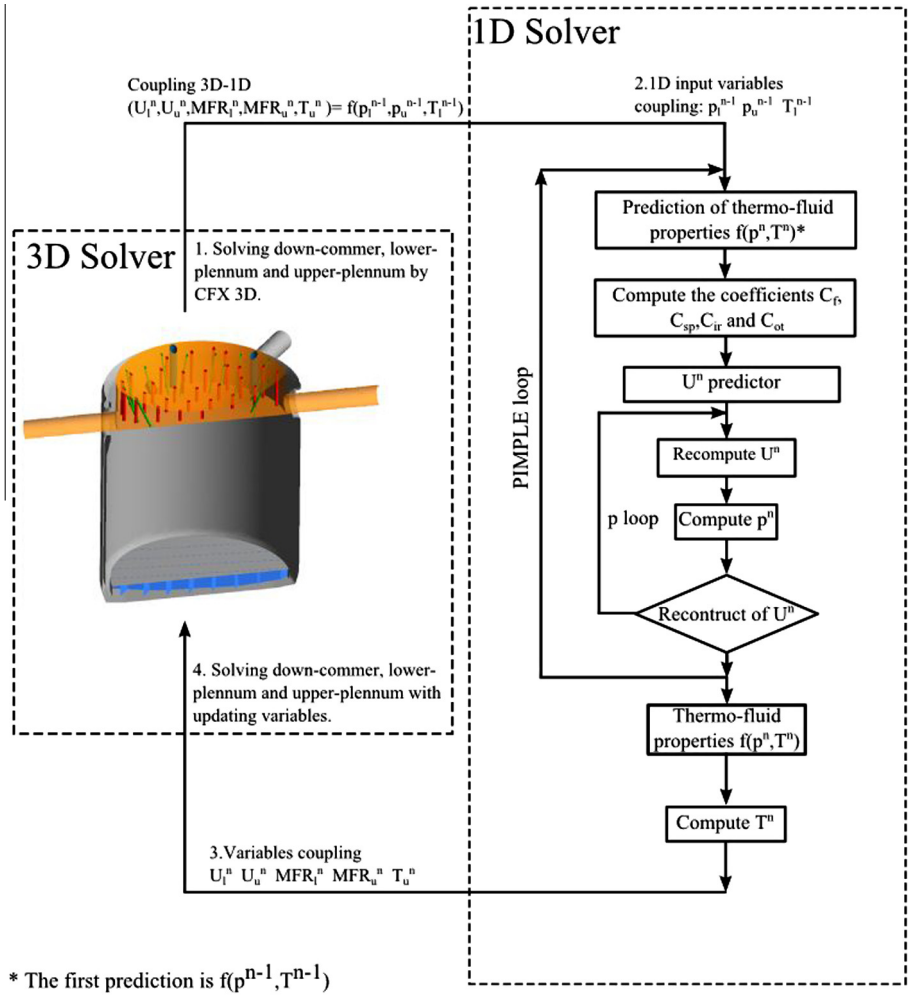

Fig. 5. Diagram of the model algorithm.

CFX which evaluates the variable *var* in the location *loc* (*loc* refers to the name assigned to the SSP). The probe function uses linear interpolation to evaluate the variable in the specific point in which this is required. In this case the locations of the corresponding SSP.

Once the 1D code solves the flow for each CC, it returns the following required information to the SSP: the absolute mass flow rate (kg/s), the temperature of the outlet mass flow, the vertical velocity and the turbulent values (k and epsilon in this case). For those SSPs that extract mass only the mass flow rate is necessary. As can be noted, no any information about the flow velocity from the 3D domain is required by the 1D code. Thus, the inlet flow entering to a 1D CC is assumed as only dominated by pressure differences. On the other hand, the in-channel flow inertial effect is implicitly taken into account by the time dependence of the 1D code formulation.

The coupling was explicit in terms of pressure and temperature. That means that the 1D code computes the CCs transport variables using the previous time step state (p_1^{n-1}, p_u^{n-1}, T_1^{n-1}, T_u^{n-1}) and then, the 3D solver updates the variables MFR, the axial velocity, and temperature received from the UFR and solves the 3D field.

The velocity and temperature profiles in the axial direction along the 451 CCs are calculated. The local mass flow rate at each CC is mainly a consequence of the pressure difference between the pair of SSPs and arises after solving the transport momentum Eq. (12). Of course, the flow-restrictor pressure losses at the channel inlets are a function of the hydraulic zones in which the core is

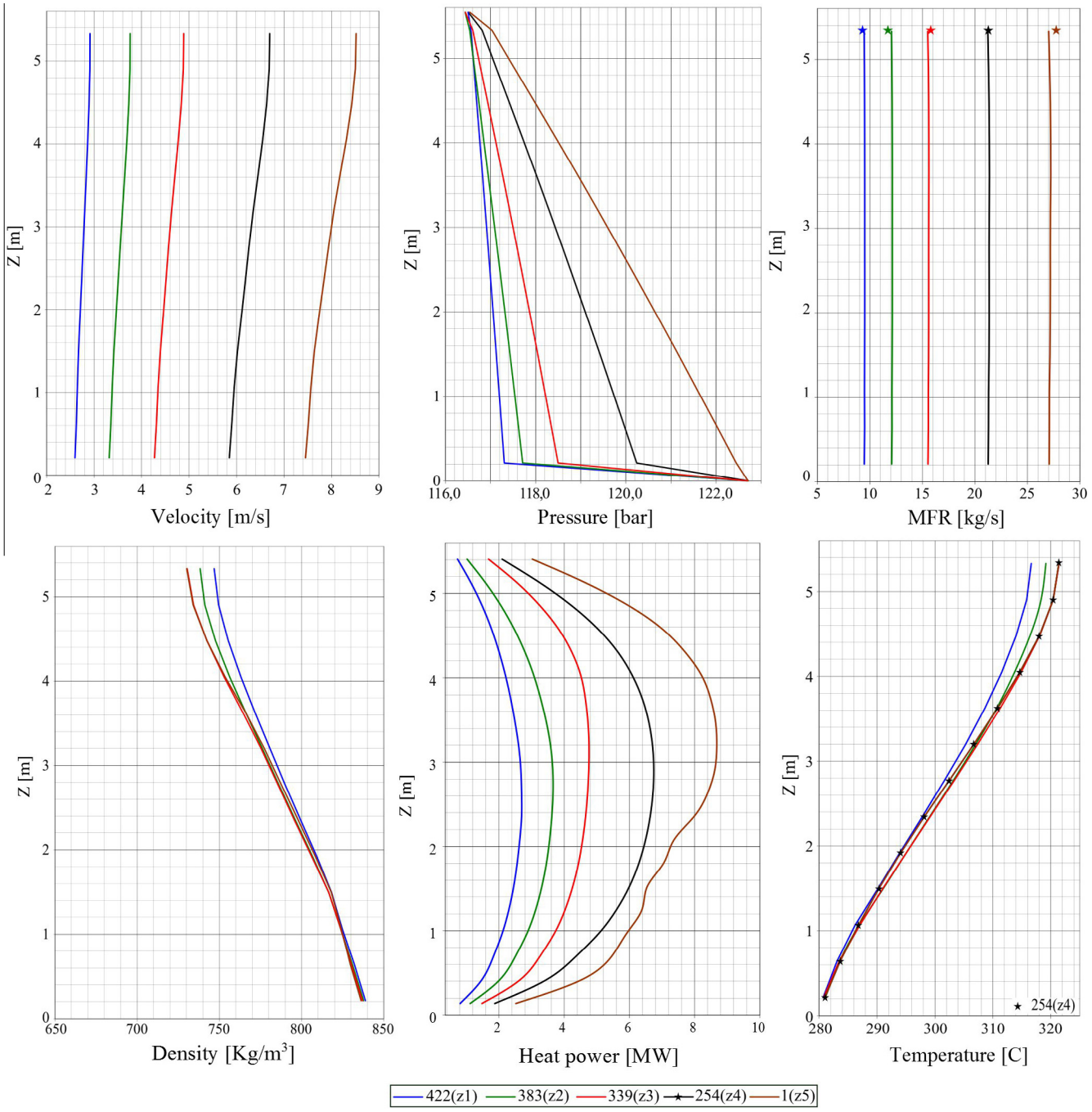

Fig. 7. 1D results for CCs: 1 (HZ:5), 254 (HZ:4), 339 (HZ:3), 383 (HZ:2) and 422 (HZ:1).

divided. Therefore, the calculated mass flow rate becomes different for each CC taking into account both the pressure field inside the upper and lower plenum and the HZ in which the CC is placed.

In the same way, the temperature profile along each CCs is obtained by solving the enthalpy transport Eq. (13) coming from the temperature probes from the pair of SSPs, the imposed axial power distribution (see Fig. 7) and the averaged channel power (Table 1). Regarding the velocity at the outlet throttle of each CC, it is calculated from the mass flow rate, the total area of the 14 vertical slots that compose the throttle and the local density. Due to the fact that the slots are homogeneously distributed along the periphery of the channel tube end, the outlet flow must be almost radially distributed. But to represent this effect by means of a single source point is not possible (only one direction must be defined for a SSP). However, the inclusion of a cylinder body above and very close of each upper SSP representing the blind tap and the mechanical coupling system for the refueling device has remedied this lack. Hence, the required radial outlet flow is obtained by the impact of a vertical flow on the cylinder body. In Fig. 5 it can be seen some of the red cylinders put in the upper plenum to represent it. The amounts of cylinders shown are less than those for the whole model because of clarity reasons.

The 3D assembly domain was meshed with 9.128.118 cells (8.819.511 tetrahedrons, 3.302 pyramids and 305.305 wedges). The lower domain composed by the cold legs, the downcomer and the lower plenum has a volume of 56.22 m^3 and was meshed with 3.934.401 elements. On the other hand, the upper domain composed by the hot legs and the upper plenum has a volume of 31.06 m^3 and was discretized with 5.193.717 elements. 1D domains of each CC were meshed with 13 elements.

Steady state simulations were performed using a time marching strategy. Relatively large time step seems to be suitable for solving the 3D model with stable and fast convergence rates. However, it must be mentioned that the 3D model and the 1D code can use different time steps allowing to employ a time sub-cycling strategy if necessary. For this particular case a pseudo time step of 5×10^{-3} s. was choice for the 3D solver while for the 1D model a time step of 1×10^{-4} s. was required to guarantee the stability of the solution and avoid the back flow during the first stage of the simulation. RMS residuals for mass and momentum were less than 5×10^{-4} while for energy and turbulence were less than 5×10^{-6} and 1×10^{-4} respectively. The mass unbalance between the lower inlet and the upper outlet was carefully kept below 1%. A high resolution scheme (Barth and Jespersen, 1989) was used for advective momentum terms and a first order upwind for turbulent quantities (ANSYS-CFX, 2010). Equations were solved using local (multicore) parallel computing facilities in one Intel(R) Core(TM) i7 CPU 950 3.07 GHz, 12 GB RAM.

5. Results and discussion

Numerical results of the steady state solutions describing the overall flow behavior of the RPV are presented in this section. The results help to evaluate the capabilities of the developed computational model, which combines the coupling strategy (SSPs) with the compressible formulation for the 1D CC modeling. Results allow to estimate features such as the MFR in each CC for comparing with the expected nominal data before the preliminary tests are made. Moreover, CFD data provides means to visualize thermal distribution in the upper plenum. Once the plant starts up and reaches the normal operation conditions the thermal stratification observed at the hot leg nozzles could be compared with temperature measurements from a set of thermocouples located at the upper and bottom sides of the ducts.

The steady state solution was achieved after few time steps. Fig. 6 shows the evolution of the MFR at the two boundary inlets (cold legs) and the two boundary outlets (hot legs). Due to stability reasons, during the first 180 iterations the 1D solver was turned off and nominal conditions for MFR and temperature were imposed at the SSPs in the 3D domain. Once the strong initial oscillations extinct the 1D solver began calculation. The necessity of introducing this startup strategy was motivated by numerical instabilities due to the non-linear nature of the dynamic pressure boundary conditions implemented in the 1D solver and also because of the loose coupling strategy adopted for the interaction between the 1D and the 3D domains.

The overall MFR for the RPV becomes very similar to the expected for nominal conditions (model underestimation is less than 3%).

Fig. 7 shows the transport variable fields along one CC of each HZ. Velocity increases along the channels due to the density reduction caused by the coolant heating and the pressure reduction. With the exception of the unthrottled HZ 5 (central CCs), the pressure drop caused by the inlet restrictor dominates over the others in-channel losses. After that, the pressure continues to decrease due to wall frictional losses and to form losses at the spacer grids. The plot at the upper right side shows the calculated MFR along with the expected one for the five HZs (star points).

The local pressure in the cells of the 1D domain of the CCs is used to calculate the saturation temperature. Results for nominal power show that the coolant remains subcooled in all CCs. The current 1D code is limited to single-phase. In consequence steam generation under subcooled cannot be estimated and only the average thermodynamic conditions can be evaluated.

Fig. 8 shows the velocity pattern over a vertical plane cutting the cold legs and horizontal planes cutting the lower and the upper plenums. The CC tubes above the SSPs are not displayed for clarity. The flow inside the upper plenum is very complex with small flow structures induced by the high velocity of the flow coming from the CCs and the presence of the 451 CC tubes as well as the control rods. Inside the annulus section of the downcomer the flow is not homogeneous with velocities ranging from 1 to 5 m/s.

Inside the lower plenum all the rhomboidal cells of the distributor show vortex structures of the size of the cells. As expected, flow velocity is rather high at the unthrottled central CCs reaching up to 2 m/s. Consequently, the maximum velocities inside the upper plenum are achieved in the central CCs and around the hot leg

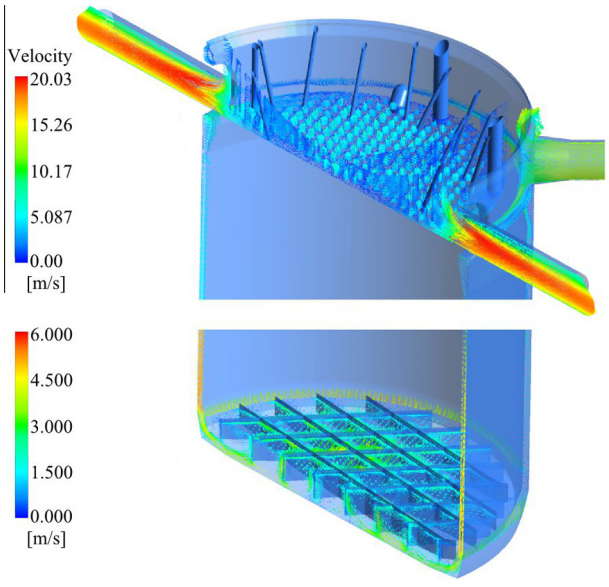

Fig. 8. Velocity pattern over some cut planes for the HW case.

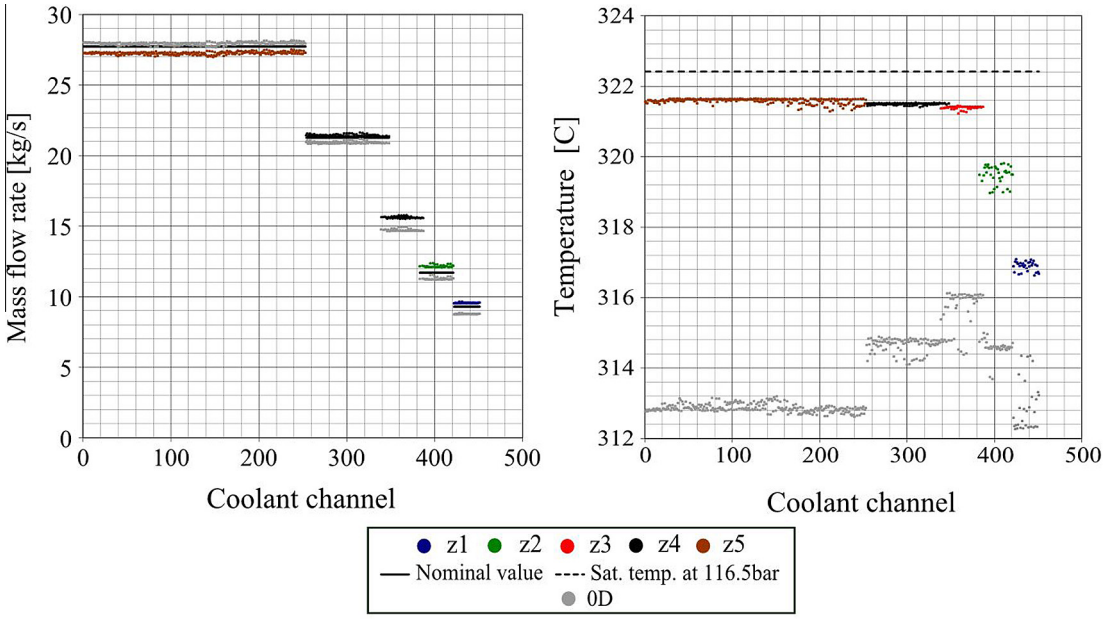

Fig. 9. Comparison between 0D and 1D models: MFR (Left side) and temperature (Right side) in upper SSP for the LW case.

mouthpieces. This flow distribution is also found for PWRs (Jeong and Han, 2008).

The results from the 0D and 1D models are compared in Fig. 9 by imposing a frozen set of boundary conditions for pressure and temperature at the CC ends (without coupling the CC code and the 3D domain). The more significant differences can be found in the in-core MFR and the outlet temperature of the CCs. The MFR for each CC for both models is showed at the left graphic. As noted, for the core center (HZ 5) the predicted MFR from the 1D code become less than from the 0D one. On the other hand, the MFR at the peripheral CCs become greater for the 1D code. The nominal MFR data is also included for comparison.

The graphic at the right in Fig. 9 shows the outlet temperature of the CCs from both models. Saturation temperature at 116.5 bar (dashed line) is included for comparison. Temperature difference between the 0D and 1D models becomes significant. For the 0D model the temperature in the HZ 5 is significantly lower than for the other HZs because of the MFR is bigger than the expected. On the other hand, the 1D model shows more homogeneous temperatures.

Fig. 10 gives insight into the velocity and the temperature profiles over a vertical plane cutting the hot legs. Note that the flow is strongly accelerated around the hot leg mouths. Mixing occurs intensively in part due to the control rods and the CC tubes above the SSPs but mainly due to the velocity of the flow coming from the SSPs. The inlet and the outlet moderator ducts have no significant effect on the flow. This is explained by the stagnant flow at the periphery of the upper plenum. It is important to notice the

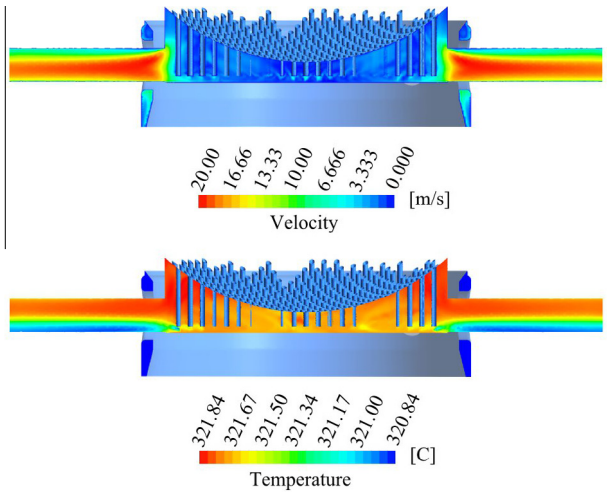

Fig. 10. Velocity (upper side) and temperature (bottom side) patterns over a plane cutting the hot legs.

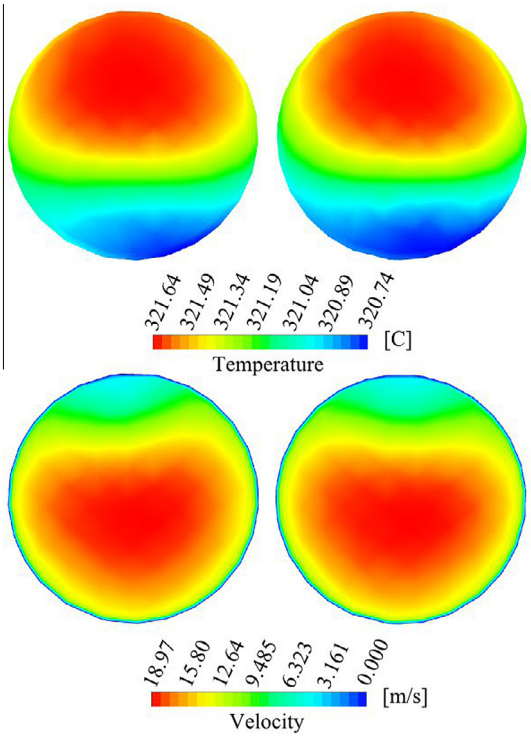

Fig. 11. Temperature (upper) and velocity (bottom) profiles at the hot leg outlets.

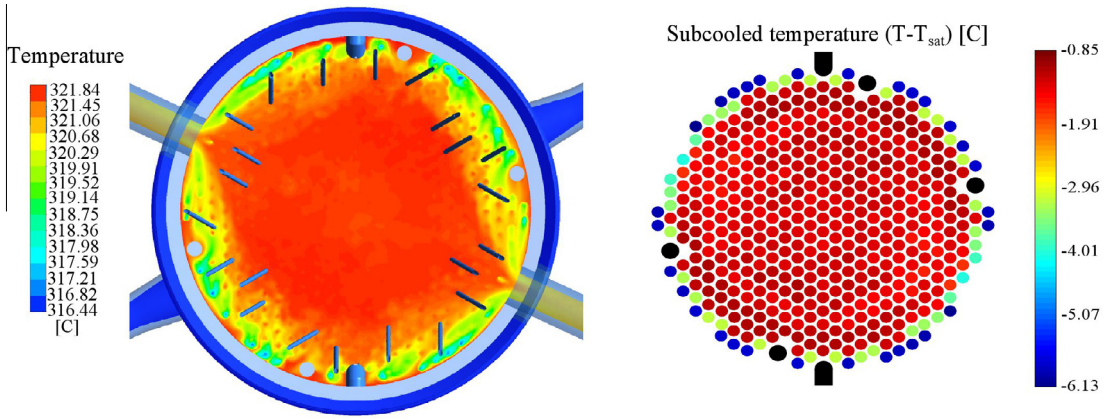

Fig. 12. Upper plenum temperature and subcooled temperature ($T - T_{sat}$) at the outlet coolant channels.

thermal stratification between the top and the bottom zones of the upper plenum. This effect, also reported by other authors (Shen et al., 2002) persists beyond the hot leg mouths as showed in the cross sectional cut planes in Fig. 10. Temperature profiles show a slight stratification of about 1 °C as can be noted in Fig. 11.

Thermal stratification occurs due to the contributions of the peripheral CCs for which the coolant heating is less intense and their flow is easily conducted to the hot legs, and poor mixing with the flow of the more heated central CCs takes place. According to the level of stratification it may be concluded that the thermo-hydraulic design is well balanced. In a recent work (Chiang et al., 2011) thermal stratification of more than 15 °C for a PWR was reported.

Fig. 12 at the left shows the temperature profiles over a horizontal plane cutting the upper plenum at the height of the upper SSPs. Note that the thermal distribution seems to have similarity with the HZ distribution. All the CC outlets are subcooled with differences of more than 5 °C between the center and the periphery. These results seem to be in good agreement with literature data (Mazzantini et al., 2010). Fig. 12 at the right shows the subcooled temperature as a measure of the degree of thermal compromise of the different CCs at the outlets SSP. Saturation conditions are defined by the local pressure at each CC. Moreover, the temperature of coolant is a compromise between the imposed local power and the estimated MFR; therefore it is more important to plot the subcooled instead of the temperature itself. For such reason, Fig. 12 shows an irregular distribution in the CC outlets with subcooled ranging from less than 1 °C to more than 6 °C.

6. Conclusions

In view of the results presented above it can be concluded that the model developed is in good agreement with the expected for nominal operation at maximum power. While considering the single-phase limitations of the present model, it should be noticed the useful information that it provides about the coolant flow in the RPV. Both LW and HW cases have not shown significant different thermo-fluid behavior. The use of LW as the coolant fluid was reflected in a slightly less subcooled than that for HW.

The 1/3D results were in accord with the ones obtained from the 0/3D in terms of the smaller pressure drop expected at the downcomer and the good efficiency of the flow distributor at the lower plenum. The 1/3D results with LW allowed to have preliminary data about the in-core flow distribution before actual in-channel mass flow measurements can be performed.

The 1/3D model allowed an estimation of the pressure drop and the coolant heating along each one of the 451 CCs. The compressible formulation offers a suitable approach to the density variations and its effect over velocity in steady state solutions.

The 1D code for modeling the CCs gave predictions about the in-core flow distribution and temperature pattern at the upper plenum which happens to be in agreement with the expected results gathered from design and literature. Due to the fact that saturation conditions are not reached, the limited single-phase model seems to be useful to characterize the RPV behavior under nominal conditions.

Future work is oriented to the implementation of a two-phase model to give a more realistic approach of the in-channel steam generation under subcooled boiling. Moreover, the modeling of pressure changes during fast transients or Loss Of Coolant Accidents (LOCA) will be assessed.

Acknowledgements

Authors want to thanks to Universidad Nacional del Litoral (CAI+D 2011 PJ 500 201101 00015 and CAI+D PI 501 201101 00435) and CONICET (PIP 112 201101 00331). Also they want to thanks to Autoridad Regulatoria Nuclear (ARN) for their financial support. Finally, thanks are owed to Nicolas Schiliuk and Alejandro Lazarte, who contributed to improving this work.

References

Adorni M., Del Nevo A., D'Auria F., Mazzantini O., 2011. A Procedure to Address the Fuel Rod Failures during LB-LOCA Transient in Atucha-2 NPP, Science and Technology of Nuclear Installations.

Ambrosini, W., Forgione, N., Ferreri, J.C., Bucci, M., 2004. The effect of wall friction in single-phase natural circulation stability at the transition between laminar and turbulent flow. Ann. Nucl. Energy 31 (16), 1833–1865, Elsevier.

Anglart, H., Nylund, O., Kurul, N., Podowski, M.Z., 1997. CFD prediction of flow and phase distribution in fuel assemblies with spacers. Nucl. Eng. Des. 177, 215–228.

ANSYS-CFX Solver Theory Guide, 2010.

Araneo, D., Ferrara, P., Moretti, F., Rossi, A., Latini, A., D'Auria, F., Mazzantini, O., 2010. Integrated software environment for pressurized thermal shock analysis. Sci. Technol. Nucl. Install.

Bae, J.H., Park, J.H., 2011. The effect of a CANDU fuel bundle geometry variation on thermal–hydraulic performance. Ann. Nucl. Energy 38 (9), 1891–1899, Elsevier.

Barth, T., Jespersen, D., 1989. The design and application of upwind schemes on unstructured meshes. AIAA 89–0366.

Bonelli, A., Mazzantini, O., Sonnenkalb, M., Caputo, M., Garcia, J.M., Zonoco, P., Gimenez, M., 2012. Station black-out analysis with MELCOR 1.8.6 code for Atucha 2 nuclear power plant. Sci. Technol. Nucl. Install.

Carlson, K., Riemke, R., Rouhani, S., Shumway, R., Weaver, W., 1990. RELAP5/MOD3CODE Manual, Volume I: Code Structure, System Models and Solution Methods. INEL Report, NUREG/CR-5535 (EGG-2596).

Chen, N.C.J., Wendel, M.W., Mark, W., Yoder, G.L., 1994. Conceptual design loss-of-coolant accident analysis for the advanced neutron source reactor. Nucl. Technol. 105 (1), 104–122. American Nuclear Society.

Chiang, J., Bau-Shei, P., Tsai, P., 2011. Pressurized water reactor (PWR) hot-leg streaming: Part 1: Computational fluid dynamics (CFD) simulations. Nucl. Eng. Des. 241 (5), 1768–1775, Elsevier.

Chun, M., Seo, K.W., 2001. An experimental study and assessment of existing friction factor correlations for wire-wrapped fuel assemblies. Ann. Nucl. Energy 28 (17), 1683–1695, Elsevier.

Corzo, S., Ramajo, D., Marquéz Damian, S., Nigro, N., 2011. CFD Simulation inside a PHWR coolant channel of the Atucha II nuclear power plant. In: ENIEF 2011, Rosario, Argentina, 2011.

Ferziger, J., Peric, M., 1999. Comp. Methods for Fluid Dynamics, Volume 3. Springer, Berlin.

Ghiaasiaan, M., 2008. Two-Phase Flow, Boiling and Condensation. Cambridge Univ. Press.

Jasak, H., 1996. Error analysis and estimation for the finite volume method with applications to fluid flows. Direct 1000 (June).

Jasak, H., Jemcov, A., Tukovic, Z., 2007. OpenFOAM: a C++ library for complex physics simulations. In: International Workshop on Coupled Methods in Numerical Dynamics, pp. 1–20.

Jeong, J.H., Han, B.S., 2008. Coolant flow field in a real geometry of PWR downcomer and lower plenum. Ann. Nucl. Energy 35 (4), 610–619.

Krepper, E., Koncar, B., Egorov, Y., 2007. CFD modeling of subcooled boiling – concept, validation and application to fuel assembly design. Nucl. Eng. Des. 237, 716–731.

Kurul N., Podowsky M., 1991. On the modeling of multidimensional effects in boiling channels. In: ANS Proc. 27th National Heat Transfer Conference, Minneapolis, MN, pp. 28–31.

Launder, B.E., Spalding, D.B., 1974. The numerical computation of turbulent flows. Comp. Meth. Appl. Mech. Eng. 3 (2), 269–289.

Lazarte, A., Fullmer, W., Bertodano, M., 2010. Experimental validation of RELAP5 and TRACE5 for licensing studies of the boron injection system of Atucha II. Sci. Technol. Nucl. Install.

Le Corre, J.M., Yao, S.C., Amon, C., 2010. A mechanistic model of critical heat flux under sub-cooled flow boiling conditions for application to one-and three-dimensional computer codes. Nucl. Eng. Des. 240, 235–244.

Lerchl, G., Austregesilo, H., 2006. ATHLET Mod 2.1 Cycle A User's Manual, Gesellchaft für Anlagen-und Reaktorsicherheit (GRS) mbH, GRS-P-1/Vol. 1, Rev. 4.

Lestani, H.A., Gonzáles, H.J., Florido, P.C., 2014. Negative power coefficient on PHWRs with CARA fuel. Nucl. Eng. Des. 270, 185–197.

Mascitti, J.A., Madariaga, M., 2011. Method of calculation of DPA in the reactor pressure vessel of Atucha II. Sci. Technol. Nucl. Install.

Mazzantini, O., Schivo, M., Di Césare, J., Garbero, R., Rivero, M., Theler, G., 2010. A coupled calculation suite for Atucha II operational transient analysis. Sci. Technol. Nucl. Install.

Moskva, Leningrad, 1960. Handbook of Hydraulic, Resistance. Goudarstv ennoe Energetic heskoeIzdateĺstvo.

Ramajo, D., Corzo, S., Schiliuk, N., Nigro, N., 2013. 3D modeling of the primary circuit in the reactor pressure vessel of a PHWR. Nucl. Eng. Des. 265, 356–365.

Rhie, C.M., Chow, W.L., 1983. Numerical study of the turbulent flow past an airfoil with trailing edge separation. AIAA J. 21 (11), 1525–1532.

Shen, X., Yu, P., Yang, G., 2002. Hydromechanical investigation on 3 PWR upper plenum core structures. Nucl. Eng. Des. 217 (1), 103–110, Elsevier.

Thurgood, M., 1983. COBRA/TRAC, A Thermal–hydraulics Code for Transient Analysis of Nuclear Reactor Vessels and Primary Coolant Systems. The Commission.

Tsuji, N., Nakano, M., Takada, E., Tokuhara, K., Ohashi, K., Okamoto, F., Tazawa, Y., Inaba, Y., Tachibana, Y., 2014. Study of the applicability of CFD calculation for HTTR reactor. Nucl. Eng. Des. 271, 564–568.

Versteeg, H., Malalasekera, W., 2007. An Introduction to Computational Fluid Dynamics: The Finite Volume Method. Prentice Hall.

Vijayan, P.K., Pilkhwal, D.S., Saha, D., Venkat Raj, V., 1999. Experimental studies on the pressure drop across the various components of a PHWR fuel channel. Exp. Therm. Fluid Sci. 20, 34–44.

Vyskocil, L., Macek, J., 2014. Coupling CFD code with system code and neutron kinetic code. Nucl. Eng. Des. 279, 210–218.

Wagner, W., Cooper, J.R., 2000. The IAPWS industrial formulation 1997 for the thermodynamic properties of water and steam. J. Eng. Gas Turbines Power 122 (1), 150–182.